Advanced Materials Technologies

ADVANCED MATERIALS TECHNOLOGIES
www.advmattechnol.com

RESEARCH ARTICLE OPEN ACCESS

Liquid Metal-Based Stretchable Strain Sensor for Fruit Growth Monitoring

Asad Ullah[1,2] | Lennert Purnal[1,2] | Maximilian Krack[1,2] | Sander Vijgen[1,2] | Thijs Vandenryt[1,2] | Dieter Reenaers[1,2] | Ronald Thoelen[1,2] | Wim Deferme[1,2]

[1]Institute For Material Research (imo-imomec), Hasselt University, Hasselt, Belgium | [2]Division (imo-imomec), IMEC, Diepenbeek, Belgium

Correspondence: Asad Ullah (asad.ullah@uhasselt.be)

Received: 7 November 2025 | **Revised:** 26 January 2026 | **Accepted:** 10 February 2026

Keywords: fruit growth monitoring | fruit thinning | liquid metal | precision agriculture | silicone elastomer | stretchable sensors

ABSTRACT

Precision agriculture (PA) increasingly relies on advanced sensing technologies to optimize crop yield, quality, and management practices. In this study, we present a stretchable strain sensor specifically designed for monitoring fruit growth ranging from 8 mm to 20 mm in diameter, a critical window for determining the timing for fruit thinning. The sensor employs a silicone elastomer (Ecoflex 00-30) as both substrate and encapsulant, and a liquid metal (LM) eutectic alloy (Galinstan) as a sensing/conductive channel. Uniform spray coating was used to deposit LM as a sensing channel. The sensor was reshaped into a cylindrical structure, which enabled conformity to the fruit surfaces. The sensor demonstrates stable electromechanical performance with resistance increasing from 2.4 ± 0.5 to $12.2 \pm 0.5\ \Omega$ under 150% strain (axial). Environmental testing confirmed durability under UV, moisture, and temperature fluctuations. A field validation test was carried out using a manual, self-built readout system. The sensor exhibits a promising response during the growth period from 8 to 20 mm. Results from the Lab and field indicate the sensor's durability and reliability, making it suitable for long-term deployment in fields/orchards. The proposed sensor offers growers actionable data to optimize thinning, irrigation, and fertilization practices by providing periodic monitoring of the fruit growth.

1 | Introduction

The demand for precision agriculture (PA) has intensified due to global challenges, including climate change, water scarcity, and the growing need to ensure food security for an increasingly populous world [1, 2]. Traditional methods for crop monitoring (particularly for fruit or vegetable growth monitoring), including manual measurements using vernier calipers and dendrometers, are often labor-intensive, time-consuming, invasive, and prone to error [3–6]. Camera-based monitoring systems, while useful, are costly and highly dependent on stable lighting conditions and unobstructed visibility, making them unsuitable for continuous field deployment [7, 8]. These limitations underscore the need for developing non-invasive, real-time, and reliable monitoring systems to support sustainable and modern agricultural practices [9–11]. Several specific sensing technologies have been demonstrated in the agricultural context. Fiber Bragg Grating (FBG) based wearable sensors have been employed for high-precision monitoring of plant growth, such as stem elongation [12]. Printed sensors using chitosan-based inks have been explored for continuous monitoring of stem elongation, offering environmentally friendly and biodegradable solutions [13]. Likewise, polymer (PDMS and Ecoflex)/metallic salt (AgNO3) stretchable strain sensors have been reported for monitoring fruit growth, particularly in apples near harvest time [14]. These works highlights the breadth of sensing strategies, but each faces limitations. FBG sensors require costly optical setups, printed sensors often lack durability under outdoor conditions, and polymer/metallic salt sensors are constrained in stretchability, making them less suitable for early-stage fruit development [15, 16].

To overcome the challenges associated with the above techniques, LM-based stretchable sensors have emerged as a compelling alternative, particularly those employing Galinstan, due to its high conductivity (~3.4×10^6 S/m), environmental stability, non-toxic nature, and excellent deformability. When LM is embedded into a soft elastomer such as silicone rubbers or thermoplastics, it forms a continuous microchannel that remains electrically stable even under large deformation, typically sustaining strains of ~400%–700% without mechanical failure [17]. In contrast, sensors made with silver nanoparticle inks (~10^5 S/m) or carbon-based composites (~10^3 S/m) typically suffer from cracking, delamination and irreversible conductivity loss at strains exceeding 50%–100%. Beyond superior electromechanical performance, recent advances in stretchable electronics [18, 19], have enabled multifuctional and intelligent sensing architectures, motivating a shift toward practical, long term applications. In this context, the integration of Galinstan within soft elastomers offers an exceptional combination of high conductivity, flexibility, stretchability and mechanical stability [20]. Moreover, their adaptability to conform to curved surfaces makes them particularly suitable for continuous monitoring of fruit growth, where considerable strain occurs as the fruit expands. Several studies have demonstrated the robustness of LM sensors under environmental stresses, making them strong candidates for agricultural deployment [21, 22]. However, their use in fruit growth monitoring has not yet been reported. Particularly, fabrication strategies for circular sensor development, stability under extreme outdoor conditions, and real-life field testing have not been investigated and/or reported.

Fruit thinning, in particular, is a critical agronomic practice that regulates crop load by removing immature fruits to enhance uniform growth and improve yield [23]. Timing is crucial during the early growth phase (fruit diameter 8–20 mm), which is the key window [24]. Accurate and continuous measurement of fruit diameter during this stage is therefore essential for yield prediction and for guiding practices such as irrigation, fertilization, and pest control [25]. LM-based stretchable strain sensors provide a practical solution, overcoming the limitations of conventional methods, such as dendrometers, by conforming securely to curved fruit surfaces and tolerating a wide range of expansion without slippage [26].

In this study, we propose an LM-based stretchable strain sensor designed for fruit growth monitoring during the thinning stage. The sensor was fabricated using silicone elastomer (Ecoflex 00–30) as both the substrate and encapsulant, with a spray-deposited LM channel serving as the conductive/sensing channel. Its cylindrical structure ensures intimate fruit contact, improving measurement accuracy. Electromechanical performance was validated under cyclic and uniaxial stretching corresponding to fruit growth from 8 to 20 mm, while environmental tests confirmed robustness under temperature, UV, and rainfall stresses. Finally, field deployment demonstrated the feasibility of the sensor for real-world agricultural monitoring.

2 | Materials and Methods

Monitoring fruit growth accurately using a stretchable sensor requires a combination of suitable materials, precise fabrication, and a clear understanding of sensor operation and its characterization till field validation (See S0). In this study, the methodology is divided into four main parts: Part A, material selection; Part B, sensor fabrication; Part C, working principle and Part D, readout system.

2.1 | Material Selection

Selection of an appropriate material is critical for ensuring stretchability, mechanical robustness, and biocompatibility with fruit surfaces. For this purpose, we evaluated several elastomeric materials, including silicone-based materials such as PDMS, Dragon Skin, and Ecoflex, and the thermoplastic elastomer styrene-ethylene-butylene-styrene (SEBS), to assess material compatibility and its effect on fruit growth. In the lab, dummy sensors from each material were characterized for different environmental impacts in QUV accelerated weathering chamber (Q-Lab QUV with UV-A lamps, at 0.76 W/m2.nm at 340 nm (8 h) with water spray (0.25 h) and condensation (3.75 h) cycles according to ISO4892-3), followed by assessment of mechanical stability with a tensile testing machine (MTS 10/M based on ISO 527 with loadcell 2 kN and speed 300 mm/min, clamp distance 60 mm and preload 0.05 N), after 10 and 20 days of exposure. In parallel, six dummy sensors from each material were deployed into the field's small-diameter fruits (~8 mm) to evaluate surface compatibility, adhesion, and ability to accommodate natural fruit expansion in the field.

Silver ink (Dycotec) printed on SEBS material and LM (Galinstan) channels encapsulated in Ecoflex were fabricated and subjected to the same QUV cycles, with electrical resistance monitored to evaluate degradation under environmental stress. After material selections and sensor fabrication further the stability and durability of the sensor was investigated in a Xenon chamber (Q-Lab Q-SUN Xenon arc tester with daylight filter Q, Xenon lamp according to ISO 4892-2 Method A, cycle B4:102 min dry and 18 min water spray at 0.51 W/m2.nm and 63°C black panel temperature). Together, these protocols enabled a comprehensive evaluation of material suitability for field deployment. The outcomes of these experiments are discussed in detail in the results and discussion section.

2.2 | Sensor Fabrication

Following the systematic material evaluation, Ecoflex 00-30 and Galinstan LM, identified as the most suitable materials, were used for sensor fabrication. Flex connectors were used for interfacing stretchable electronics with rigid electronics. The flex connector used in this work is a commercial flexible circuit connector fabricated by JLCPCB, which enables reliable electrical interfacing between soft, stretchable conductors and rigid electronic components. This commercial connector is based on patented design by our group [27] which was developed to ensure robust electrical and mechanical integration between soft and rigid electronics. In preparation of materials, the silicone elastomer Ecoflex 00-30, parts A and B were prepared with a 1:1 ratio and mixed using a speed mixer (DAC 150 SP SpeedMixer) at a speed of 2000 RPM for 60 s. Then the samples were degassed to remove any bubbles (using a vacuum chamber for ~20 min), and casted/injected into a 3D-printed mold. The substrate was cured for approximately 20

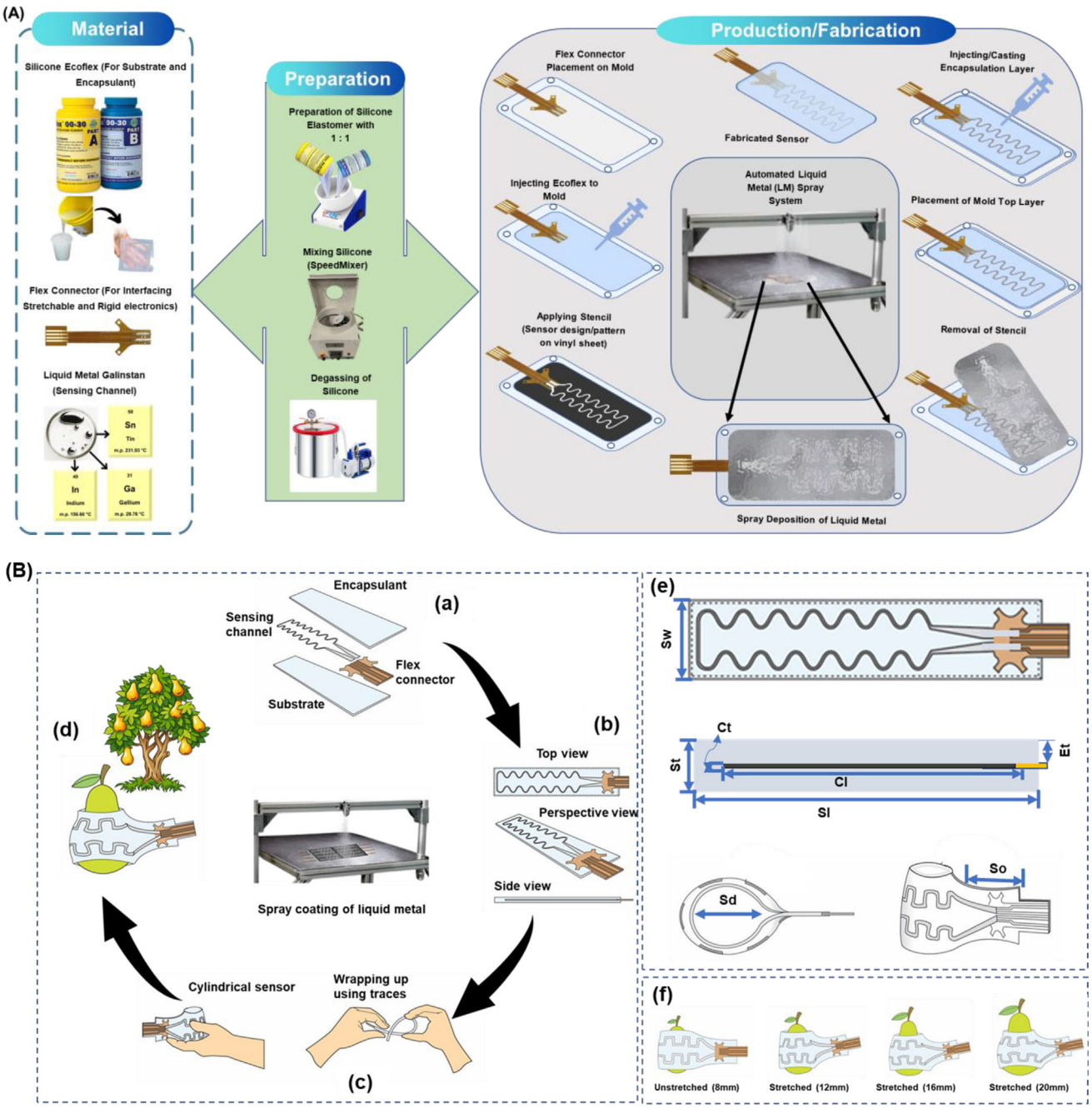

FIGURE 1 | (A) Fabrication workflow of the stretchable LM based strain sensor, illustrating material selection, silicone preparation, stencil assisted LM spray deposition, and final encapsulation. (B) Schematic representation of the sensor: Design, structural layout, and deployment concept of the stretchable sensor for fruit growth monitoring. (a) Layer-by-layer architecture showing substrate, sensing channel, encapsulant, and the flex connector. (b) Sensor geometry from different orientations (top, side, and perspective views). (c) Convert the planar sensor into a cylindrical configuration and a wrapping strategy for attachment. (d) Practical illustration of the sensor integration on fruit for monitoring diameter expansion during growth. (e) Dimensional analysis of the sensor, highlighting the dimensional overview of the planar and cylindrical sensors. (f) Conceptual demonstration of continuous fruit growth monitoring enabled by a sensor over developmental stages.

min in an oven (50°C). After curing a stencil (vinyl sheet) with the sensor design/pattern, was placed on the substrate, and LM was deposited using an automated spray system, as reported in [28] to ensure uniform coverage. The stencil was then removed, leaving a patterned conductive channel. An encapsulant layer of Ecoflex was cast over the channel to protect it from mechanical and environmental effects while maintaining stretchability. The step-by-step production/fabrication of the stretchable strain sensor is illustrated in Figure 1A. Figure 1B-a shows the sensor's main components and a multilayered overview.

Figure 1B-b shows a different view of the fabricated sensor. To conform the sensor to the fruit surface, the planar sensor was converted into a cylindrical shape for ease of integration. Converting the sensor from a planar to a cylindrical shape, small traces were made in the sensor near the flex connector and at

the end of the sensing channel, and were wrapped around while holding it in a cylindrical shape, as shown in Figure 1B-c. In this configuration, the sensor was sealed with Ecoflex at the point of connection. A heat gun (dryer) was used at approximately 300°C for ~30 s to achieve rapid curing of the sample resulting in a smooth drying process and a perfect cylindrical shape. This process resulted in conformal, mechanically stable sensors that adhered reliably to the fruit surfaces as illustrated in Figure 1B-d. Compared to traditional or conventional rigid sensors, such as dendrometers, which lack stability on dynamic surfaces, this strategy improves adhesion and stability and reduces obstruction during fruit growth [29]. Figure 1B-e represents the dimensional views of the fabricated sensors. Here, *'Sl, Sw, St'* represent the length, width, and thickness of the fabricated sensor, which are 70, 25, and 1.5 mm, respectively. Similarly, *'Cl, Cw, Ct'* represent the length, width, and thickness of the LM sensing channel, which is 40, 0.7, and 30 µm. *'Et'* represents the encapsulant thickness, which is 0.67 mm. For the cylindrical-shaped sensor, the diameter *'Sd'* is 8 mm and the open area (outside the cylindrical shape) *'So'* is 25 mm, providing as such a strain relief at the flex connector to ensure that fruit growth primarily acts on the sensing channel rather than the connector region.

The fabricated sensor was tested using a four-probe measurement device, Keithley (2400) to verify the resistance values in the relaxed state and under stretching. The sensor was further characterized through different tests, including cyclic tests (uniaxial and axial stretching, with a strain limit of up to 150% at a step size of 2 mm s^{-1} (3.33% s^{-1})), to investigate its stability, which is essential for fruit growth monitoring in the real field case. The complete characterization is further explained in the results and discussion section.

2.3 | Working Principle

A strain gauge sensor operates on the principle of resistance changes induced by mechanical deformations. When an external force is applied to a material, it undergoes strain, leading to slight changes in its dimensions. These dimensional changes affect the strain gauge's electrical resistance, which is typically made of a wire or conductive channel [30]. In fruit growth monitoring, a strain gauge sensor detects a slight deformation as the fruit expands over time.

This is illustrated in Figure 1B-f, which shows how the sensor will behave toward different stretched levels, that is, 8 (0%), 12 (50%), 16 (100%), and 20 mm (150%). The sensor, made from a conductive material, LM embedded in a silicone elastomer, changes its electrical resistance when subjected to mechanical strain. The resistance R of the sensor is given by:

$$R = \rho \frac{L}{A} \tag{1}$$

where *'ρ'* is the resistivity of the LM, *'L'* is the sensor's length, and *'A'* is its cross-sectional area. In the context of fruit growth, increasing the Turgor pressure within the fruit cells results in gradual surface expansion [31], which is captured by the conformal strain sensor. As the fruit grows, it exerts a tensile strain on the sensor, increasing *'L'* while decreasing *'A'*, resulting in a measurable increase in resistance *'R'*. The strain *'ε'* is defined as:

$$\varepsilon = \frac{\Delta L}{L} \tag{2}$$

The gauge factor (GF), which relates the resistance change to the applied strain, is given by:

$$GF = \frac{\frac{\Delta R}{R}}{\varepsilon} \tag{3}$$

By integrating the stretchable strain gauge sensor with a wireless readout system, real-time monitoring of fruit growth can be achieved.

2.4 | Read-Out System

A stable read-out system is essential for accurately and precisely measuring the resistance changes in a stretchable sensor. Two common approaches are used for strain sensors, including the series resistor and constant current source methods [32]. In the series resistor method, a fixed resistor is placed in series with the sensor, and the voltage across the sensor is measured.

The resistance can be calculated using Ohm's law. However, this method is sensitive to variations in power supply voltage and requires precise calibration, making it less reliable for measuring low resistances. On the other hand, the constant current source method provides a more stable and accurate solution, as it ensures a fixed current through the sensor regardless of changes in its resistance [33].

Thus, we utilize a constant current source readout system for our stretchable sensor, as the sensors base resistance at 0% stretch is 2.4 ± 0.5 Ω, and at 150% stretch (axial), it reaches up to 12.2 ± 0.5 Ω. This method supplies a precise, low-magnitude current (e.g., 1 or 10 mA) through the sensor while measuring the resulting voltage. The resistance is then determined using Ohm's law. The key advantage of using a constant current source for resistance measurement is its ability to minimize errors resulting from wire resistance and voltage fluctuations. This approach ensures a stable current supply, enabling precise resistance measurement. A current source (high precision) can be employed to implement this method, using an IC or OpAmp-based circuit. Furthermore, a high-resolution ADC (16 or 24-bit) is used to measure the voltage drop across the sensors ensuring accurate resistance measurement [34]. Since the sensor's base or initial resistance is low, selecting a high-resolution ADC is crucial for improving measurement accuracy.

Figure 2 shows the block diagram and electrical design of the read-out system used for the measurements. The current source is implemented using an NCP1117LP, from Onsemi, America, a voltage regulator. This regulator stabilizes a voltage of 1.8 V between pin 1 and 4. With a 180 Ω feedback resistor, the circuit produces a stable output current of approximately 10 mA. Due to tolerance in the feedback resistor and minor inaccuracies in the regulated voltage, the actual current may deviate by up to 5% from the nominal 10 mA. Nevertheless, the current remains

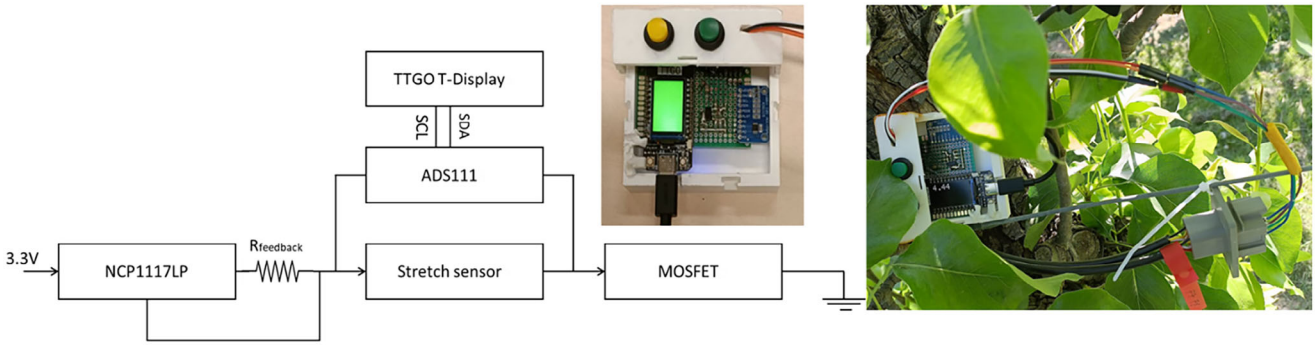

FIGURE 2 | Readout electronics for resistance measurement showing its block diagram and visuals of the manual portable measurement readout system.

stable, with a fluctuation of only ±0.001 mA within a load range of 2 Ω to 40 Ω. Once characterized, the current source provides a reliable basis for precise resistance measurements. Voltage is measured with an ADS1115, a 16-bit analog-to-digital converter (ADC) operating with a chosen gain of 8.

The resolution is calculated using the following formula;

$$\frac{Umax - Umin}{(2^{bit-size}) \times gain} = \frac{6.114V - (-6,114V)}{2^{16} \times 8} = 0.41108 \text{ V}$$

When combined with the stability of the current source, the theoretical accuracy can be calculated with the error propagation formula.

$$\frac{\Delta R}{R} = \frac{\Delta U}{U} + \frac{\Delta I}{I}$$

$$\Delta R = \left(\frac{\Delta U}{I \times R} + \frac{\Delta I}{I} \right) \times R \tag{4}$$

With ΔU equal to 0.41108 V, I equal to 10.2770 mA, ΔI equal to ±0.001 mA, and R in the range of 2 Ω to 40 Ω. The worst-case accuracy is within ±0.006 Ω.

3 | Results and Discussion

This section presents a comprehensive investigation of the proposed stretchable sensor, beginning with the material characterization and selection outcomes, environmental effects on the sensor performance, mechanical durability and tensile testing, sensor's electromechanical response (toward uniaxial and axial strain), and finally, field validation to demonstrate the sensors practical applicability for monitoring fruit growth.

3.1 | Material Characterization and Selection

The comparative analysis revealed significant differences in environmental durability and field compatibility among the tested materials. Under accelerated weathering, Ecoflex 00-30 exhibited stable mechanical performance. It maintains high stretchability and tensile resilience even after 20 days of QUV exposure, which resembles 1 year in a real environment for elastomeric polymers [35]. For reference, fresh samples were first tested before QUV exposure. Ecoflex stretched up to 750% with a maximum stress of 163 kPa. In comparison, Dragon Skin, PDMS, and SEBS reached elongations of 583%, 113%, and 960%, respectively, with maximum stresses of 367, 430, and 1020 kPa, respectively (see S1(c)(d)). After 10 and 20 days of QUV exposure, SEBS was completely degraded, becoming brittle and sticky (see S1(b)). Ecoflex, Dragon Skin, and PDMS also exhibited signs of degradation after prolonged exposure. However, the extent of deterioration varied among them. Ecoflex, Dragon Skin and PDMS are silicone elastomers with a Si-O backbone, while SEBS is a thermoplastic elastomer with an organic hydrocarbon backbone. Ecoflex and Dragon Skin are both platinum-cured PDMS elastomers, but their formulation differs in crosslink density, side groups, and filler content [36]. In Ecoflex, the crosslinking is more uniform and a low filler content leads to reduced localized defect sites where UV initiated degradation start. In soft silicones (Ecoflex) the low cross link density and high chain mobility allows these minor chemical changes to be accommodated without significant mechanical deterioration. In contrast, stiffer silicone (Dragon Skin and PDMS) networks exhibit greater stress localization under UV combines with thermal, and moisture cycling followed by tensile test, resulting in more noticeable degradation [37–39]. Finally, the SEBS thermoplastic elastomer absorbs UV radiation. This, combined with thermal and moisture effects, leads to radical formation and photo oxidative chain scission which results in mechanical embrittlement [40]. As shown in the tensile results (see S1(e-f)), Ecoflex retained a greater proportion of its original stretchability and mechanical strength compared to the other elastomers, which showed more pronounced reductions in both stress and strain at break. These results demonstrate that Ecoflex 00-30 is more reliable and durable even under accelerated QUV exposure. Since the QUV chamber represents an environment comparable to natural conditions (depending on the materials being characterized) [41], the sensor is expected to operate reliably for at least one fruit growth season under real field exposure.

Field experiments for materials (Ecoflex, Dragon Skin, PDMS, and SEBS) reinforced these observations. Dummy sensors made from PDMS, Dragon Skin, and SEBS which were attached to the fruit, frequently fell from the tree within a few days, failing to accommodate the expansion of the growing fruit. Conversely, Ecoflex sensors remained intact throughout the observation

period, stretching seamlessly with fruit growth, without causing any damage to the fruit (see S2). This behavior aligns with Ecoflex's reported ability to undergo strains exceeding 500% without mechanical failure [42, 43].

For the conductive channel, Dycotec based silver ink printed on SEBS degraded rapidly under QUV conditions, with increased resistance and partial track/channel failure (see S1(b)). LM-based samples, on the other hand, maintained a stable response throughout the exposure. Overall, both laboratory and field investigations, demonstrate that Ecoflex 00-30, combined with Galinstan as the sensing channel, provides stable responses, compatibility with fruit skin, and environmental robustness. This combination was therefore selected as the final substrate, sensing channel, and encapsulation strategy for the stretchable fruit growth sensor.

3.2 | Environmental Characterization

After material selection, the fabricated Ecoflex-Galinstan stretchable sensors were subjected to environmental stability tests. These tests are crucial, as the sensor is intended for long-term monitoring in field applications. To evaluate this aspect, the sensors were systematically tested under controlled temperature, outdoor conditions, and Xenon aging testing.

3.2.1 | Thermal Characterization (Temperature Effect)

The influence of temperature on the sensor's response was investigated for both relaxed and stretched configurations (in cylindrical shape). The sensor was characterized by placing it in an oven. For LM-based sensors, the response is linear over the temperature range from 20°C to 60°C and back to 20°C, in steps of 2°C. As shown in the Figure 3a, the relaxed sensor exhibits a slight but consistent resistance increase with rising temperature from 20°C to 60°C with a nearly reversible trend upon cooling. A similar trend was observed for the stretched sensor, as shown in the Figure 3b, where the sensor resistance was higher due to strain (strain applied by the inflated balloon), but the relative change with temperature followed the same profile. Although the experimental characterization was limited to 20°C–60°C, the observed linearity and reversibility enable reliable extrapolation to lower temperatures, which is consistent with previously reported work, showing that galinstan electrodes maintain high electrical conductivity and stable electrical performance even under large deformation (mechanical) up to 130% strain, even below 0°C [44].

Generally, the response of any stretchable sensor, is affected by both strain and temperature [45]. Considering the temperature effect:

$$\mathrm{R\,(T)} = \mathrm{R_o} \times (1 + \alpha \Delta \mathrm{T}) \tag{5}$$

$R(T)$ is the resistance under temperature change, *'Ro'* is the initial resistance measured at reference temperature without applied strain, *'ΔT'* represents the temperature change from that reference state, and finally 'α' is the temperature coefficient of resistance, which indicates how the resistance responds to a unit change in temperature. The temperature sensitivity can be quantified using the temperature coefficient of resistance (TCR), defined as:

$$\mathrm{TCR} = \alpha = \frac{1}{\mathrm{R_o}} \frac{\Delta \mathrm{R}}{\Delta \mathrm{T}} \tag{6}$$

ΔR is the change in resistance, and ΔT is the change in temperature. From the Figure 3a, using the above formula, the TCR for the relaxed sensor is calculated as 1.12×10^{-3} $(^{\circ}\mathrm{C})^{-1}$, and for the stretched sensor, the TCR is 1.10×10^{-3} $(^{\circ}\mathrm{C})^{-1}$, which is in line with value $(1.2 \times 10^{-3}(^{\circ}\mathrm{C})^{-1}$ reported in literature [46].

The $\Delta R/\Delta T$ was calculated as 3.15×10^{-3} $\Omega(^{\circ}\mathrm{C})^{-1}$, and 12.525×10^{-3} $\Omega(^{\circ}\mathrm{C})^{-1}$, for relaxed and stretched states respectively. The near-overlapping heating and cooling curves indicate good reversibility and negligible thermal hysteresis, suggesting that the conductive sensing channel remains stable across the entire temperature range tested.

3.2.2 | Xenon Chamber Test

To evaluate the durability and effectiveness of the sensors under various environmental conditions such as humidity, temperature, water spraying and solar irradiation, accelerated aging experiments were conducted in a Xenon chamber using the sensors in a relaxed, static state. Multiple sensors were tested, and their resistance was recorded over 30 days, as shown in Figure 3c. The results revealed excellent stability, with resistance variations remaining within ±5% across all samples.

3.2.3 | Outdoor Test

In addition to thermal characterization, the outdoor performance of the sensors was evaluated by mounting multiple sensors onto 3D-printed pear-shaped designs with different diameters, that is, 8 mm (0%), 12 mm (50%), 16 mm (100%), and 20 mm (150%). Continuous resistance monitoring over 6 weeks (42 days) was recorded, demonstrating a stable response for each diameter as shown in Figure 3d. To assess long-term stability, the variation in resistance was quantified using Equation 7.

$$Stability\ (\%) = \frac{Rmax - Rmin}{Rmean} \times 100 \tag{7}$$

where R_{max} and R_{min} are the maximum and minimum resistance values measured during the monitoring period, and R_{mean} is the average resistance. Based on this analysis, the stability values were 4.90% for the 8 mm sensor, 8.37% for the 12 mm stretched sensor, 6.75% for the 16 mm stretched sensor, and 9.84% for the 20 mm stretched sensor. These results confirm that, although minor fluctuations were observed, the sensors maintained consistent performance throughout long-term outdoor exposure. The observed stability values remain relatively small and would not significantly affect performance in many practical real-time monitoring scenarios [47, 48].

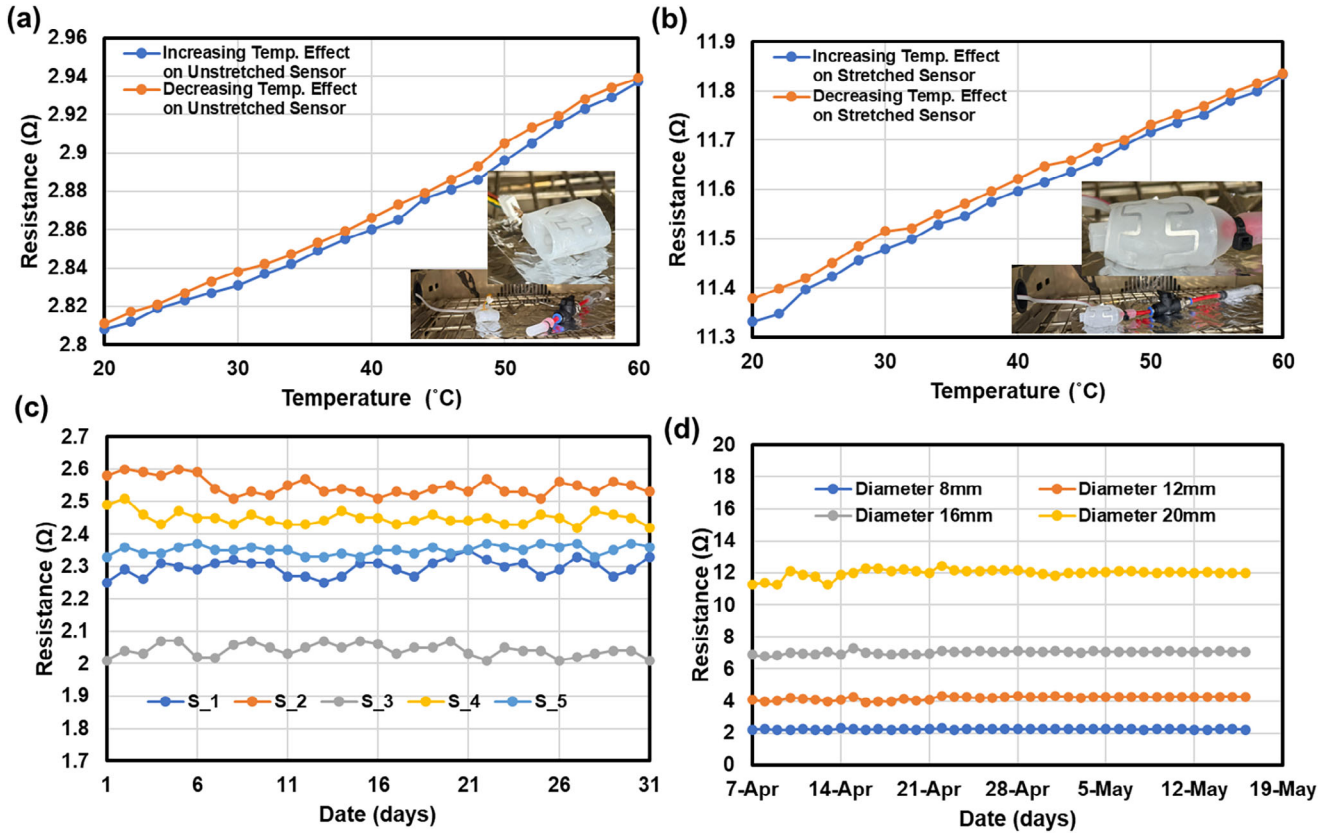

FIGURE 3 | Thermal and environmental stability of the stretchable sensors. (a,b) Temperature-dependent resistance under relaxed and stretched states. (c) Accelerated aging in a Xenon chamber, with resistance stability for various sensors during prolonged exposure. (d) Outdoor deployment of sensors with long-term resistance of sensors using a 3D pear model having varying diameters.

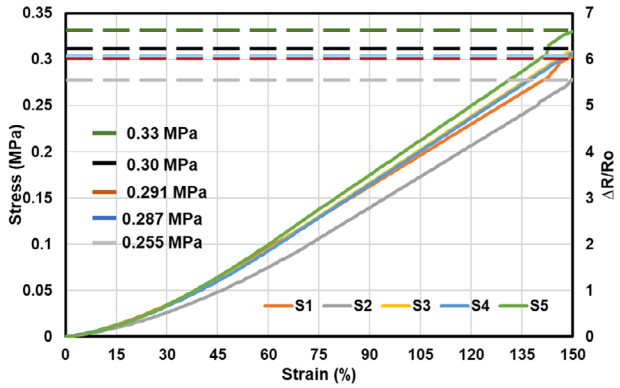

FIGURE 4 | Mechanical stability, resistance-strain, and stress-strain behavior of five sensors, Low stress range (0.255–0.33 MPa) demonstrates sensor compliance, ensuring negligible resistance against fruit growth forces.

3.3 | Mechanical Stability

The mechanical characterization of the sensors was carried out using a tensile testing machine to compare the sensors ability to withstand deformation caused by the Turgor pressure exerted by the fruit on the sensor. The samples were fitted into the clamp (60 mm) by keeping both upper and lower jigs parallel, and the loading speed was set to 300 mm/min with a preload of 0.05 N (see S3). The tensile stress-strain curve in Figure 4 provides critical insights into the mechanical robustness of the Ecoflex-based sensor. The maximum stress values for the tested sensors ranged from 0.255 MPa to 0.33 MPa at strains of up to 150%. For the cylindrical shape ring, these stress values become lower than that. By using Hoop stress (circumferential stress):

$$\sigma\theta = p\frac{r}{t} \tag{8}$$

Here '$\sigma\theta$' is the Hoop stress/pressure exerted on the sensor (tensile), which is 0.33 MPa (maximum) in our case, 'r' is the radius of the cylinder, which is 4 mm, and 't' is the thickness of the cylindrical wall, which is 2 mm, ';p' represent the pressure exerted on the sensor (cylindrical). To calculate p, we have:

$$p = \frac{t \times \sigma\theta}{r}$$

$$p = 0.165\ \text{MPa}\ (\text{for}\ 0.33\ \text{MPa tensile test})$$

This stress level is considerably lower than the pressure typically exerted by growing fruits on their outer surface because of the cell divisions (Turgor pressure), and it is stronger when the fruit is in the fruit set and maturation stage, that is, (8–20 mm). This Turgor pressure in the fruit tissue is generally around 0.6 MPa for pear.

At the cellular level, it exceeds up to ~3 MPa, which represents the internal hydrostatic pressure driving cell expansion during growth [49, 50]. The fact that the sensor stress response is comparably lower than the physiological stresses present inside pears suggests that the sensor can adapt to natural fruit growth without imposing excessive mechanical constraints [50, 51].

The relatively low stress levels also indicate that the sensor material, primarily stretchable elastomer, can deform easily in response to external expansion without resisting fruit growth. In other words, as the fruit grows and exerts outward force, the sensor accommodates the deformation by stretching rather than opposing the natural growth process. This feature is vital for agricultural applications, since any rigid or mechanical-resistant sensor (such as is the case in a dendrometer) could resist the fruit expansion, resulting in inaccurate data or even fruit surface damage [52–56].

3.4 | Sensor Response to Strain

3.4.1 | Uniaxial Stretching

The experiments above demonstrate the compatibility of the selected materials and the final fabricated sensor with fruit growth. In the next section, experiments are discussed in which the sensor, in its final circular form, is tested for strain sensing. However, to establish the fundamental electromechanical performance of the sensor, its response to externally applied strain was first investigated under controlled uniaxial stretching. This provides a baseline understanding of sensitivity, hysteresis, and repeatability before adapting the device for axial deformation. Figure 5 illustrates the uniaxial stretching performance of the fabricated stretchable planar sensor. The experimental characterization setup, in which the sensors are mounted on a uniaxial testing setup and electrically connected for electromechanical stretching tests, is presented in S4. The sensors were fixed at a distance of 64 mm (initial sensor length, that is, 0% strain) in relaxed mode, and then the sensor was stretched to a controlled, targeted strain of up to 160 mm (150% strain) with a step size of 2 mm. This configuration ensures uniform loading along the stretching direction, allowing accurate evaluation of strain-dependent resistance variations. The resistance response of the sensor under increasing strain is shown in Figure 5a, where normalized resistance (R/Ro) exhibits a nearly linear increase up to 150% strain.

The coefficient of determination ($R^2 = 0.9739$) confirms the correlation between strain and resistance changes. A more detailed analysis of the sensitivity at different strain levels is provided in Figure 5b, where the Gauge factor is calculated according to Equation 3. Since precise and repeatable readings are crucial in precision agriculture applications, the sensor's resistance and strain connection are steady and predictable. Based on the sensor size, the Gauge factor (GF) indicates how responsive the sensor is to strain. The sensor demonstrates increasing GF values with strain, ranging from approximately 2.23 at 30% strain to 3.59 at 150% strain, indicating enhanced sensitivity under large deformation. Such values are in line with what is typically observed for LM-based strain sensors [45, 46], where resistance changes mainly result from geometric deformation of the conductive channel sensor, which is applicable for thinning application [49], to monitor the fruit growth from 8 to 20 mm (strain limit from 0%–150% calculated using Equation 2).

The hysteresis curve is shown in Figure 5c,d, where the difference between loading (stretching) and unloading (relaxed state) is quantified for a complete cycle and point by point. Point-by-point hysteresis is defined as:

$$H(\varepsilon) = \frac{|Rloading(\varepsilon) - Runloading(\varepsilon)|}{Rmax} \quad (9)$$

With the *Rloading* and *Runloading* representing the resistance at a given strain during stretching and relaxed state, respectively, and *Rmax* is the maximum resistance in a cycle. From Figure 5c our observed hysteresis was recorded as 2.38% for 0%–150% strain (complete cycle). From Figure 5d (point by point hysteresis) it is shown that at low strain (0%–40%), hysteresis grows steadily (~0.1% to 2.1%), at the intermediate strain (80%–120%), hysteresis peaks (~3% to 3.4%), after 120% strain, the hysteresis starts to shrink again, and at 150% it is 0 (because both loading and unloading curves meet at the maximum stretch).

In strain sensors, low hysteresis is a key indicator of stability, since it ensures that the sensor returns to nearly the same resistance for a given strain during both stretching and relaxing. Here, point-based hysteresis was calculated, ranging from 0% to 3.5% at maximum across a strain of 0%–150%. Therefore, the hysteresis values fall within the expected range for LM-based sensors [51–53], indicating that the sensor exhibits stable and efficient response characteristics.

Further, a cyclic test was performed to assess the repeatability and stability of the sensor for multiple stretch cycles (10 cycles, primarily to verify the sensor repeatability, although the sensor is intended for one-time use in the field), as shown in the Figure 5e,f. In Figure 5e, three sensor samples were subjected to 10 consecutive stretching and relaxing cycles. All exhibited consistent resistance-strain responses with a negligible drift, confirming the reproducibility and reusability of the sensor for multiple tests. These results confirm the use of such sensors for multiple seasons. Figure 5f further demonstrates cyclic durability where relative resistance of the sensor repeatedly increases and decreases over 10 loading and unloading cycles for strains of 150%. No significant degradation in the sensors performance was noted. The inset highlights a single cycle of stretching and relaxing. Together, these results verify that the planar sensor can withstand large uniaxial deformations with high sensitivity, stability, and repeatability.

3.4.2 | Sensor Testing on Balloon Phantom Model

Following the uniaxial stretching tests, evaluating the sensor under conditions that more closely resemble fruit growth typically involves radial expansion rather than purely linear deformation. To provide initial insights into this experiment, a preliminary balloon model using only Ecoflex was investigated (see S5). Although this simple phantom confirmed the feasibility of tracking axial expansion, it also revealed key limitations. In particular, the low modulus of Ecoflex led to circumferential

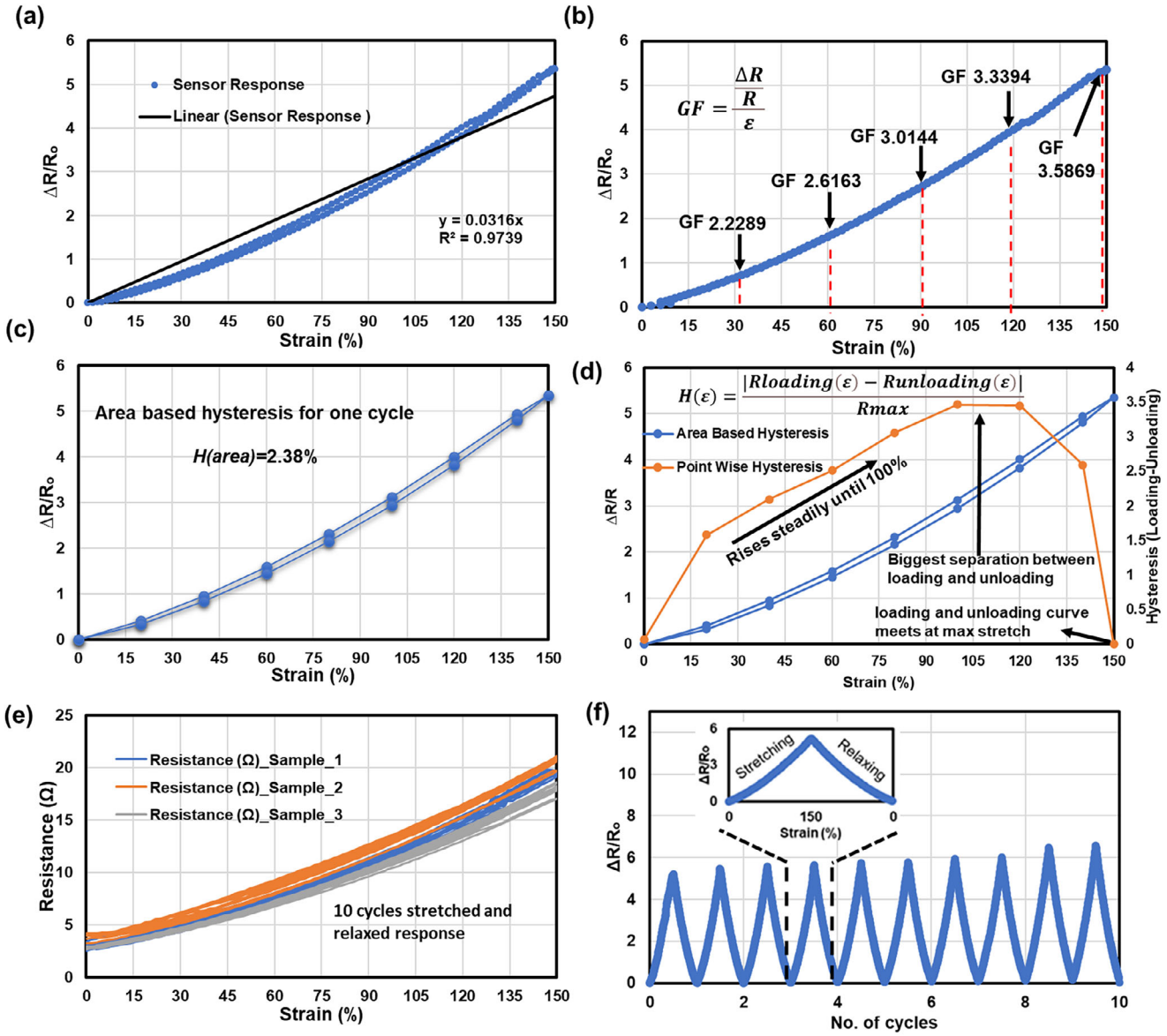

FIGURE 5 | Sensor uniaxial stretching characterization (a) Relative resistance changes as a function of strain with linear fitting and coefficient of determination. (b) Sensitivity analysis showing the calculated gauge factor across different strain ranges. (c) Hysteresis analysis for a complete cycle. (d) Hysteresis behavior during loading and unloading cycles is plotted point by point against the strain. (e) Resistance strain curves of four samples subjected to 10 repeated stretching and releasing cycles, demonstrating reproducibility. (f) Cyclic durability test up to 10 cycles, showing consistent resistance response; the inset illustrates stretching and relaxing profiles.

deformation during the late stage of inflation, producing a saturation effect that reduced strain sensitivity and narrowed the effective sensing window. These findings emphasized the need for a more controlled design that can deliver stable strain transfer.

To mimic axial stretching more precisely, we must overcome the challenges faced in the previous case (see S5). Which reduce the usable sensing window and limit the sensors reliability for applications where stable and proportional strain transfer is critical.

Therefore, a hybrid balloon structure was developed by integrating two different materials, that is, Ecoflex (softer material) and Dragon Skin (stiffer material). In this design, Dragon Skin forms reinforcing bands on the upper and lower regions, while Ecoflex is used in the central expansion zone where the sensor is attached. The balloon is pre-stretched to remove the initial stretching effects. Upon inflation, the Dragon Skin regions resist deformation due to their higher modulus, directing internal pressure toward the softer Ecoflex window. This controlled strain localization eliminates late-stage saturation, ensuring sensor stretching occurs consistently across the 8–20 mm diameter range.

The experimental characterization of the sensor using the hybrid balloon design is presented in the Figure 6a,b. In Figure 6a, the results demonstrate that the device provides reproducible strain transfer with relatively low variability across repeated trials for n = 7 independent sensors, with a standard deviation of ±2% at higher strain values. The sensor's relative

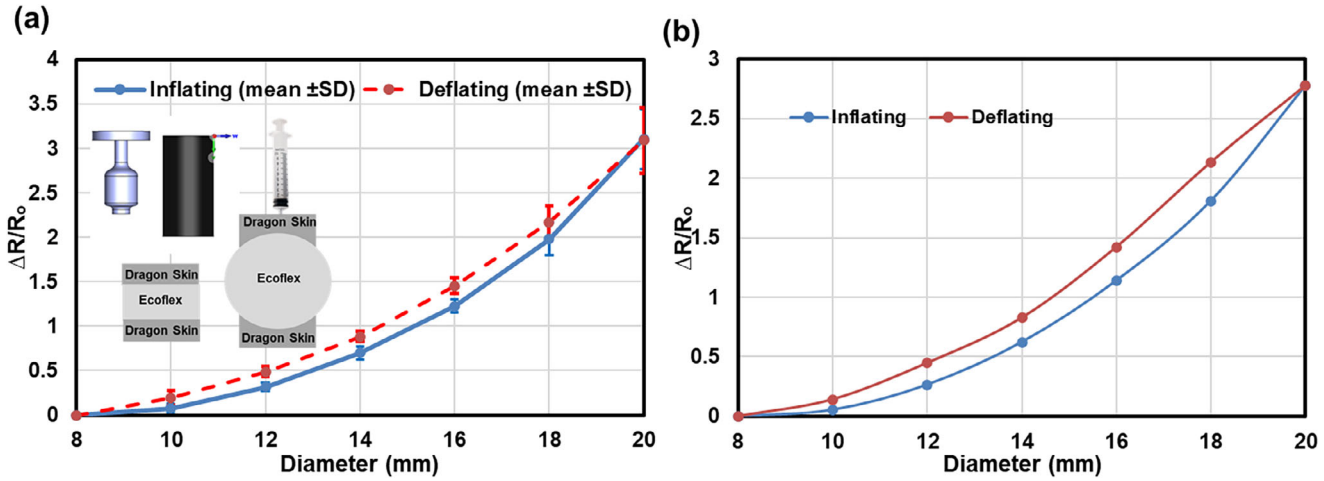

FIGURE 6 | Sensor characterization on soft balloon-shaped actuator to mimic the fruit growth (a) Averages across multiple sensors trials (n = 7, mean ± SD), confirming reproducibility and reduced variability in the hybrid structure, with inset shows the design and fabrication of soft hybrid actuator using Ecofex and Dragon Skin (b) Sensor hysteresis analysis between inflation and deflation cycles.

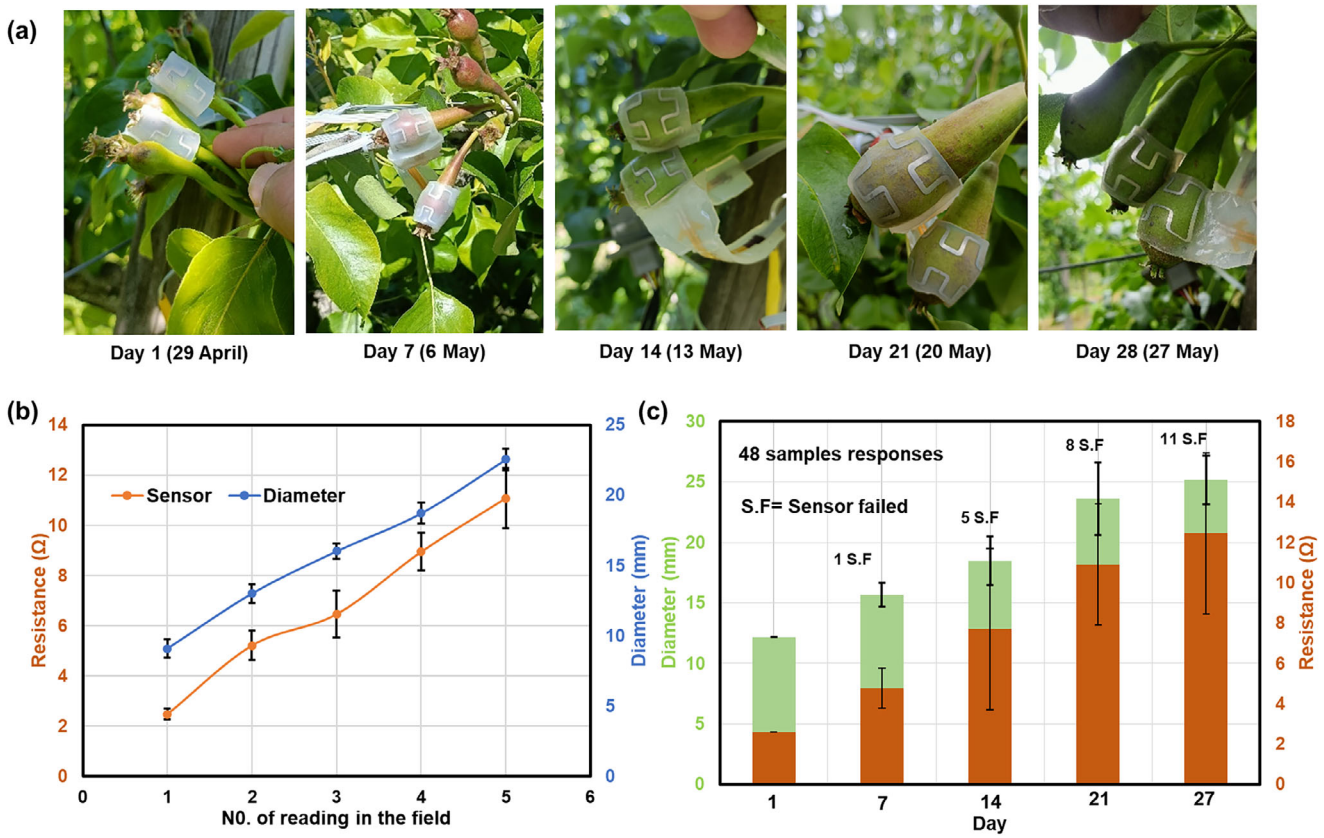

FIGURE 7 | Field deployment of stretchable sensors for real-time fruit growth monitoring. (a) Sequential images of the sensor integration on pear fruitlets over a 28-day growth period. (b) Correlation between the resistance change of four representative sensors and the corresponding fruit diameter measured with a vernier caliper. (c) The statistical summary of 48 deployed sensors highlights both functional devices and sensor failures due to connector detachment or environmental degradation during stretching.

response is shown, exhibiting a progressive increase with diameter, which confirms effective strain localization within the Ecoflex window. The inflation-deflation comparison reveals a measurable hysteresis loop, as shown in Figure 6b, (which is much improved compared to the Ecoflex balloon case (see S5(b)). The hysteresis remains within a moderate range, indicating that Dragon Skin reinforcements control the circumferential deformation that was prevalent in the earlier single-material (Ecoflex) balloons. Overall, these results demonstrate that the hybrid balloon design provides a controlled and predictable strain field, making it suitable for reliable sensing applications.

TABLE 1 | Comparison of the previous studies with the presented research work.

Refs.	Material and sensor principle	Application focus	Max Strain	Temp. range	Limitations	Gap filled by this work
[12]	Fiber Bragg Grating wearable sensor	Plant growth monitoring	—	22°C and 38°C	Rigid integration, require optical readout, costly	Current work provides a low cost, conformal, with electronic readout system
[13]	Chitosan-based water ink (mixing graphite powder and chitosan solution) flexible strain sensor	Plant growth monitoring (stem expansion)	Maximum strain up to 60%	—	Not fruit specific, no field validation.	Current work targets fruit growth (8–20 mm) with real orchard validation
[14]	Polymer/metallic salt stretchable strain sensor	Fruit growth monitoring (apples) targeted the harvest period	Linear resistance up to 30% strain	70°C	Material not fully durable for outdoors, limited long term data	Current work uses ecoflex+Galinstan with full environmental (UV, temp, rain spray testing)
[58]	Prestretched PDMS and Ti/Au as main metal film	Plant growth monitoring	Linear resistance up to 22%	—	Less environmental durability, short term usage	Our work expands to orchard conditions with long term robustness
[57]	Adaptive winding strain sensor (mechanical actuator inspired), integrated electronics.	Plant 'pulse'/physiological dynamic monitoring	—	15°C–30°C	Interface adaptability challenges on hairy/waxy surface, scale up to orchard untested	Our work targets fruit growth with conformal attachment and orchard trials.
[59]	Integrated wearable ring sensors (electronic readout) for high throughput surface extension measurement.	High throughput phenotyping/growth decoding across many plants	Maximum strain up to 100%	5°C–50°C	Early stage need validation across different fruit sizes and harsh outdoor weather.	Our sensor focuses on small fruit range and explicitly reports environmental stress testing in real orchard.
This work	Ecoflex 00-30 elastomer +Galinstan liquid metal	Fruit growth monitoring for a critical growth stage (8–20 mm)	For the reported application 150% (normally upto 750%)	20°C–60°C	Connector failure (future work will focus on the connector improvement)	First demonstration of cylindrical, conformal stretchable LM elastomer based sensor validated in real orchard conditions.

3.5 | Sensors Validation in the Field

Following material selection, environmental and mechanical stability, and electromechanical characterization, the sensors were deployed for real-time fruit (pear) growth monitoring under field conditions to monitor the fruit growth from 8 mm to 20 mm. The sensing mechanism is based on contact based sensing (sensor stretched with the growing fruit). Owing to the stretchable and conformal nature the sensor can adapt to fruits with varying curvature and mechanical properties. Consequently the sensor can be applied to other fruits such as apples without requiring structural/design modification. Fruits with higher irregular, or textured surfaces may introduce local contact variations, however such effects can be mitigated through calibration, and sensor placement. Pears were selected in this study as a representative model due to their availability and relative uniform surface. Figure 7a shows the sensor stretching with the growing fruit (from fruitlets to different growth stages). Over the 4 weeks, the sensor maintained intimate contact with the fruit surface, conforming to changes in fruit curvature and diameter. This confirms the stretchable sensor architecture's ability to accommodate fruit's natural dynamic growth in orchard conditions.

Field resistance measurements were obtained using a manual readout system at weekly intervals during day time, minimizing the influence of short term day time temperature variations. The correlation between the sensor resistance and the measured fruit diameter is summarized in Figure 7b. Four representative fruit sensor pairs were monitored, showing a consistent increase in normalized resistance as the fruit diameter increased from ∼8 mm to ∼20 mm. The resistance versus diameter relationship was monotonic across all cases, indicating that the sensor deformation closely followed the expansion of the fruit. Notably, the resistance trend across multiple sensors exhibited minor variations attributed to slight differences in mounting position and fruit surface morphology. Nevertheless, the trend confirms that the sensor reliably translates radial growth into an electrical resistance suitable for continuous tracking of fruit growth.

To evaluate the reproducibility and robustness at scale, 48 sensors were deployed in the orchard, and their performance statistics are summarized in the Figure 7c. From the 48 sensors, 11 failed during the monitoring period, with failure causes including detachment of the flex connector, and mechanical disconnection. After a complete measurement interval, the failure rate corresponds to ∼23%, which highlights the necessity of improving the flex connector [57, 27] adhesion and using strain relief at the connector point. However, the remaining 37 sensors (77%) functioned reliably, and their resistance changes showed strong agreement with the measured fruit diameter, demonstrating the scalability and robustness of the approach. Together, these results demonstrate that the stretchable sensor can be practically integrated for real-time monitoring of fruit growth, providing continuous, non-destructive, and quantitative assessment of fruit growth. Table 1 shows the comparison of our work with previous studies.

The present manuscript is the first to demonstrate an Ecoflex-Galinstan-based cylindrical sensor specifically designed for monitoring fruit growth, targeting the early fruit growth from 8 to 20 mm for improved orchard management, timely performing thinning, and high yield production.

4 | Conclusion

This work presents the design, fabrication, and validation of a stretchable strain sensor tailored for monitoring fruit growth during the thinning stage (8–20 mm). The sensor was fabricated using Ecoflex 00-30 as a biocompatible stretchable elastomeric substrate and encapsulant, and Galinstan LM as a sensing channel. The sensor achieved high stretchability, durability, and conformal integration with curved fruit surfaces. The sensor shows a consistent electromechanical performance, with resistances rising from 2.4 ± 0.5 to 12.2 ± 0.5 Ω under 150% strain (axially) and a Gauge factor increasing from ∼2.2 at 30% strain to ∼3.6 at 150% strain. The sensor exhibits low hysteresis of 2.38% for a complete cycle (0%–150% strain), and mechanical stability with stress values between 0.255–0.33 MPa, which is well below the fruit Turgor pressures, confirming that it does not hinder natural fruit growth. Environmental evaluation shows excellent stability, with resistance drift of only 2.7%–5.6% over 6 weeks outdoors and variation within ±5% after 30 days in Xenon aging tests. Field deployment on 48 pear fruitlets confirmed practical feasibility, 77% of the devices functioned reliably, and the resistance changes tracked fruit expansion from 8 to 20 mm.

Beyond its immediate application in horticulture, the proposed sensor highlights the broader potential of stretchable sensing for precision agriculture. The modular fabrication approach and low-cost materials make it scalable for large scale deployment, while its adaptability suggests feasibility for integration with wireless IoT based monitoring readout systems. Future work can extend this system by embedding autonomous readout circuitry, enhancing connector reliability, and exploring multi-sensor arrays to capture spatial growth dynamics across orchards.

Overall, the presented stretchable strain sensor represents a significant step toward data driven crop management, bridging the gap between plant physiology and digital agriculture. This technology provides growers with actionable data for thinning, irrigation, and fertilization while supporting sustainable, and high-yield farming practices.

Acknowledgements

The authors want to thank the funding organizations for their crucial contribution to enable this research work. This includes the personal funding for Maximilian Krack provided by the Fonds Wetenschappelijk Onder- zoek (FWO, 1SH1C24N) as well as the supporting bench fee provided by the Bijzonder Onderzoeksfonds (BOF, BOF23INCENT17). The authors also thank FWO for providing funding within the broader SBO project of SUBLIME (S007423N), enabling a research network across a wide range of faculties. Finally, the authors would like to thank Interreg Vlaanderen-Nederland for the funding in the project ADaM & PreciLa and the province of Limburg in Belgium for the co-financing within this project.

Funding

The authors acknowledge the support provided by the Vlaanderen-Nederland Interreg project Adam&Prescila (https://interregvlaned.eu/en/adam-precila/over-ons), SBO project of SUBLIME (S007423N), and F.W.O Personal funding for Maximilian Krack provided by the Fonds Wetenschappelijk Onderzoek (FWO,

1SH1C24N) as well as the supporting bench fee provided by the Bijzonder Onderzoeksfonds (BOF, BOF23INCENT17).

Conflicts of Interest

The authors declare no conflicts of interest.

Data Availability Statement

The data that support the findings of this study are available from the corresponding author upon reasonable request.

References

1. S. Getahun, H. Kefale, and Y. Gelaye, "Application of Precision Agriculture Technologies for Sustainable Crop Production and Environmental Sustainability: A Systematic Review," *The Scientific World Journal* 2024, no. 1 (2024): 2126734, https://doi.org/10.1155/2024/2126734.

2. S. S. Gangurde, R. Kumar, A. K. Pandey, et al., "Climate-Smart Groundnuts for Achieving High Productivity and Improved Quality: Current Status, Challenges, and Opportunities," *Genomic Designing of Climate-Smart Oilseed Crops* (2019): 133–172.

3. L. He, W. Fang, G. Zhao, et al., "Fruit Yield Prediction and Estimation in Orchards: A state-of-the-Art Comprehensive Review for Both Direct and Indirect Methods," *Computers and Electronics in Agriculture* 195 (2022): 106812, https://doi.org/10.1016/j.compag.2022.106812.

4. B. Lanza, "Development of Optical Measurement Methodologies for In-Field Estimation of Plant Health and Agricultural Yield" (PhD diss., University of Brescia, 2025), https://iris.unibs.it/handle/11379/626147.

5. A. Carella, P. T. Bulacio Fischer, R. Massenti, and R. Lo Bianco, "Continuous Plant-Based and Remote Sensing for Determination of Fruit Tree Water Status," *Horticulturae* 10, no. 5 (2024): 516, https://doi.org/10.3390/horticulturae10050516.

6. N. Ismail and O. A. Malik, "Real-Time Visual Inspection System for Grading Fruits Using Computer Vision and Deep Learning Techniques," *Information Processing in Agriculture* 9 (2022): 24–37, https://doi.org/10.1016/j.inpa.2021.01.005.

7. M. Soltani Firouz and H. Sardari, "Defect Detection in Fruit and Vegetables by Using Machine Vision Systems and Image Processing," *Food Engineering Reviews* 14, no. 3 (2022): 353–379, https://doi.org/10.1007/s12393-022-09307-1.

8. A. McCarthy, C. Hedley, and A. El-Naggar, "Machine Vision for Camera-based Horticulture Crop Growth Monitoring," in PA17-The International Tri-Conference for Precision Agriculture in 2017: Book of Abstracts (University of Southern Queensland, 2017).

9. K. Hu, Y. Cai, Z. Wang, Z. Zhang, J. Xian, and C. Zhang, "A Review on Metal Oxide Semiconductor-Based Chemo-Resistive Ethylene Sensors for Agricultural Applications," *Chemosensors* 12, no. 1 (2024): 13, https://doi.org/10.3390/chemosensors12010013.

10. D. A. Basterrechea, J. Rocher, L. Parra, and J. Lloret, "Development of Inductive Sensor for Control Gate Opening of an Agricultural Irrigation System," in 2020 Fifth International Conference on Fog and Mobile Edge Computing (FMEC) (IEEE, 2020), 250–255, https://doi.org/10.1109/FMEC49853.2020.9144810.

11. Y. Wang, X. Jin, J. Zheng, et al., "An Energy-efficient Classification System for Peach Ripeness Using YOLOv4 and Flexible Piezoelectric Sensor," *Computers and Electronics in Agriculture* 210 (2023): 107909.

12. D. Lo Presti, J. Di Tocco, S. Cimini, et al., "Plant Growth Monitoring: Design, Fabrication, and Feasibility Assessment of Wearable Sensors Based on Fiber Bragg Gratings," *Sensors* 23, no. 1 (2022): 361, https://doi.org/10.3390/s23010361.

13. W. Tang, T. Yan, J. Ping, J. Wu, and Y. Ying, "Rapid Fabrication of Flexible and Stretchable Strain Sensor by Chitosan-Based Water Ink for Plants Growth Monitoring," *Advanced Materials Technologies* 2, no. 7 (2017): 1700021, https://doi.org/10.1002/admt.201700021.

14. H. J. Lee, R. Joyce, and J. Lee, "Liquid Polymer/Metallic Salt-based Stretchable Strain Sensor to Evaluate Fruit Growth," *ACS Applied Materials & Interfaces* 14, no. 4 (2022): 5983–5994, https://doi.org/10.1021/acsami.1c21376.

15. M. I. Abdulraheem, Y. Xiong, W. Zhang, H. Chen, H. Zhang, and J. Hu, "Recent Applications of fiber Bragg Grating Sensors in Humidity and Water Content Detection in Agriculture: A Comprehensive Review of Development, Challenges, and Future Trends," *International Journal of Precision Engineering and Manufacturing* 25, no. 7 (2024): 1499–1524, https://doi.org/10.1007/s12541-024-01015-6.

16. C. Kuruppuarachchi, F. Kulsoom, H. Ibrahim, H. Khan, A. Zahid, and M. Sher, "Advancements in Plant Wearable Sensors," *Computers and Electronics in Agriculture* 229 (2025): 109778, https://doi.org/10.1016/j.compag.2024.109778.

17. J. Qin, D. Cui, L. Ren, W. Hao, Y. Shi, and Y. Du, "Emerging Advances of Liquid Metal Toward Flexible Sensors," *Advanced Materials Technologies* 9, no. 14 (2024): 2300431.

18. X. Liao, W. Song, X. Zhang, et al., "An Artificial Peripheral Neural System Based on Highly Stretchable and Integrated Multifunctional Sensors," *Advanced Functional Materials* 31, no. 24 (2021): 2101107, https://doi.org/10.1002/adfm.202101107.

19. Z. Huang, H. Chen, Y. Luo, et al., "In-Device Topological Encoding for Intelligent Multimodal Interactions," *Advanced Functional Materials* (2025): 15750.

20. C. Yang, B. Xu, Y. Tang, et al., "Super Weather-Resistant and Self-Healing Eutectogels via Dynamic Interactions for Wide-Range Healthcare and Highly Adaptive Human–Machine Interfaces," *Advanced Functional Materials* (2025): 07051.

21. M. Aarif K. O., A. Alam, and Y. Hotak, "Smart Sensor Technologies Shaping the Future of Precision Agriculture: Recent Advances and Future Outlooks," *Journal of Sensors* 2025, no. 1 (2025): 2460098, https://doi.org/10.1155/js/2460098.

22. M. Baharfar and K. Kalantar-Zadeh, "Emerging Role of Liquid Metals in Sensing," *ACS sensors* 7, no. 2 (2022): 386–408, https://doi.org/10.1021/acssensors.1c02606.

23. D. Greene and G. Costa, "Fruit Thinning in Pome-and Stone-Fruit: State of the Art," *Acta Horticulturae* 998 (2012), 93–102.

24. T. Webster, "Current Approved Thinning Strategies for Apples and Pears and Recent Thinning Research Trials in Europe," *The Compact Fruit Tree* 35, no. 3 (2002): 73–76.

25. A. Gonkiewicz, J. Blaszczyk, and A. Basak, "Chemical Pear Fruit Thinning," *Journal of Fruit and Ornamental Plant Research* 19, no. 1 (2011): 73–78.

26. W. D. Wheeler, *Fruit Tree Responses to Water Stress: Automated Physiological Measurements and Rootstock Responses (Doctoral Dissertation)* (Utah State University, 2020).

27. S. Nagels, "Interconnect, an Electronic Assembly and a Method for Manufacturing an Electronic Assembly," *US Patent* 11, no. 856 (2022): 692B2.

28. M. Krack, R. N. Sangma, L. Purnal, et al., "Process and Property Assessment of Liquid Metal Spray Deposition Towards Scalable and Reliable Stretchable Electronics," *Scientific Reports* 15, no. 1 (2025): 35984, https://doi.org/10.1038/s41598-025-19775-0.

29. T. Rose, N. Ali, and Y. Dong, "Design and Development of an IoT-Based Dendrometer System for Real-Time Trunk Diameter Monitoring of Christmas trees," *Smart Agricultural Technology* 10 (2025): 100765.

30. D. D. L. Chung, "A Critical Review of Piezoresistivity and Its Application in Electrical-Resistance-Based Strain Sensing," *Journal of Materials Science* 55, no. 32 (2020): 15367–15396, https://doi.org/10.1007/s10853-020-05099-z.

31. O. Ali, I. Cheddadi, B. Landrein, and Y. Long, "Revisiting the Relationship Between Turgor Pressure and Plant Cell Growth," *New Phytologist* 238, no. 1 (2023): 62–69, https://doi.org/10.1111/nph.18683.

32. Y. Zhao, Y. Liu, Y. Li, and Q. Hao, "Development and Application of Resistance Strain Force Sensors," *Sensors* 20, no. 20 (2020): 5826, https://doi.org/10.3390/s20205826.

33. R. Pallas-Areny and J. G. Webster, *Sensors and Signal Conditioning* (John Wiley & Sons, 2012).

34. D. W. Upton, R. P. Haigh, P. J. Mather, et al., "Gated Pipelined Folding ADC-Based Low Power Sensor for Large-scale Radiometric Partial Discharge Monitoring," *IEEE Sensors Journal* 20, no. 14 (2020): 7826–7836, https://doi.org/10.1109/JSEN.2020.2982576.

35. G. R. Fedor and P. J. Brennan, Comparison Between Natural Weathering and Fluorescent UV Exposures. Technical Bulletin LU-8035 (Q-LAB Corporation, 2011).

36. F. Virlogeux, D. Bianchini, F. Delor-Jestin, M. Baba, and J. Lacoste, "Evaluation of Cross-Linking After Accelerated Photo-Ageing of Silicone Rubber," *Polymer International* 53, no. 2 (2004): 163–168, https://doi.org/10.1002/pi.1329.

37. R. Y. Wang, Z. F. Dou, H. S. Li, N. Li, X. R. Liu, and W. F. Zhang, "Degradation Behavior and Aging Mechanisms of Silicone Rubber Under Ultraviolet-Thermal-Humidity Coupling in Simulated Tropical Marine Atmospheric Environment," *Polymer* (2025): 128398.

38. S. Zeng, W. Li, and W. He, "Effects of Combined UV-Tensile Aging on Structural and Electrical Properties of High Temperature Vulcanized Silicone Rubber in Composite Insulators," *RSC Advances* 15 (2025), 27177–27186.

39. P. N. Eleni, M. K. Krokida, and G. L. Polyzois, "The Effect of Artificial Accelerated Weathering on the Mechanical Properties of Maxillofacial Polymers PDMS and CPE," *Biomedical Materials* 4, no. 3 (2009): 035001, https://doi.org/10.1088/1748-6041/4/3/035001.

40. D. Garcia-Garcia, J. E. Crespo-Amorós, F. Parres, and M. D. Samper, "Influence of Ultraviolet Radiation Exposure Time on Styrene-Ethylene-Butadiene-Styrene (SEBS) Copolymer," *Polymers* 12, no. 4 (2020): 862, https://doi.org/10.3390/polym12040862.

41. M. Frigione and A. Rodríguez-Prieto, "Can Accelerated Aging Procedures Predict the Long Term Behavior of Polymers Exposed to Different Environments?," *Polymers* 13, no. 16 (2021): 2688, https://doi.org/10.3390/polym13162688.

42. R. Janardhana, F. Akram, Z. Guler, A. Adaval, and N. Jackson, "A Comprehensive Experimental, Simulation, and Characterization Mechanical Analysis of Ecoflex and Its Formulation under Uniaxial Testing," *Materials* 18, no. 13 (2025): 3037, https://doi.org/10.3390/ma18133037.

43. M. D. Dickey, "Stretchable and Soft Electronics Using Liquid Metals," *Advanced Materials* 29, no. 27 (2017): 1606425, https://doi.org/10.1002/adma.201606425.

44. P. Xiao, J. H. Kim, and S. Seo, "Flexible and Stretchable Liquid Metal Electrodes Working at Sub-zero Temperature and Their Applications," *Materials* 14, no. 15 (2021): 4313, https://doi.org/10.3390/ma14154313.

45. M. X. Li, D. Y. Wu, R. Y. Tang, et al., "Liquid Metal Integrated PU/CNT Fibrous Membrane for Human Health Monitoring," *Frontiers in Bioengineering and Biotechnology* 11 (2023): 1169411.

46. M. J. V. Lourenço, M. Alves, J. M. Serra, C. A. Nieto de Castro, and M. H. Buschmann, "The Thermal Conductivity of Near-Eutectic Galinstan ($Ga_{68.4}In_{21.5}Sn_{10}$) Molten Alloy," *International Journal of Thermophysics* 45, no. 1 (2024): 6.

47. S. C. Biazatti, R. Môra, M. S. V. Sccoti, J. F. de Brito Júnior, N. dos Santos Queiroz, and R. de Angeli Curto, "Criterion Dendrometer as a Non-Destructive Method for Dendrometric Estimations of Native Species in Western Amazon," *Revista Ibero-Americana de Ciências Ambientais* 11, no. 6 (2020): 59–70, https://doi.org/10.6008/CBPC2179-6858.2020.006.0006.

48. H. Z. Yousaf, M. Javed, M. M. Bashir, R. A. Shaukat, and H. Mahmood, "Highly Stable and Temperature-Independent Humidity Sensor Based on PEO/PVA Polymer Composite," *Journal of Composites Science* 9, no. 2 (2025): 85, https://doi.org/10.3390/jcs9020085.

49. W. Fricke, *Turgor Pressure* (eLS, 2017), 1–6.

50. D. J. Cosgrove, "Wall Relaxation and the Driving Forces for Cell Expansive Growth," *Plant Physiology* 84, no. 3 (1987): 561–564, https://doi.org/10.1104/pp.84.3.561.

51. G. Li, S. Liu, Z. Xu, J. Guo, S. Y. Tang, and X. Ma, "Recent Advancements in Liquid Metal Enabled Flexible and Wearable Biosensors," *Soft Science* 3, no. 4 (2023): 37.

52. J. Chen, J. Zhang, Z. Luo, et al., "Superelastic, Sensitive, and Low Hysteresis Flexible Strain Sensor Based on Wave-Patterned Liquid Metal for Human Activity Monitoring," *ACS Applied Materials & Interfaces* 12, no. 19 (2020): 22200–22211, https://doi.org/10.1021/acsami.0c04709.

53. Y. Wu, Y. Zhou, and W. Asghar, "Liquid Metal-Based Strain Sensor With Ultralow Detection Limit for Human–Machine Interface Applications," *Advanced Intelligent Systems* 3 (2021), 2000235.

54. P. Zhang, J. Fu, M. Liu, et al., "Liquid-Metal-Based Stretchable Dual-Parameter Sensor for Simultaneous Detection of Deformation and Temperature," *Advanced Materials Technologies* 8, no. 5 (2023): 2201264, https://doi.org/10.1002/admt.202201264.

55. M. Olszacki, C. Maj, M. Al Bahri, et al., "Experimental Verification of Temperature Coefficients of Resistance for Uniformly Doped P-Type Resistors in SOI," *Journal of Micromechanics and Microengineering* 20, no. 6 (2010): 064008, https://doi.org/10.1088/0960-1317/20/6/064008.

56. A. Khosravi, E. M. Lodolini, V. Giorgi, F. Belluccini, A. Mancini, and D. Neri, "Continuous Proximal Monitoring of Diameter Variation From Root to Fruit," *Horticulturae* 11, no. 6 (2025): 635, https://doi.org/10.3390/horticulturae11060635.

57. C. Zhang, C. Zhang, X. Wu, J. Ping, and Y. Ying, "An Integrated and Robust Plant Pulse Monitoring System Based on Biomimetic Wearable Sensor," *npj Flexible Electronics* 6, no. 1 (2022): 43.

58. J. M. Nassar, S. M. Khan, D. R. Villalva, M. M. Nour, A. S. Almuslem, and M. M. Hussain, "Compliant Plant Wearables for Localized Microclimate and Plant Growth Monitoring," *npj Flexible Electronics* 24, no. 1 (2018): 24, https://doi.org/10.1038/s41528-018-0039-8.

59. T. Sun, C. Lu, Z. Shi, et al., "PlantRing: A High-throughput Wearable Sensor System for Decoding Plant Growth, Water Relations, and Innovating Irrigation," *Plant Communications* 6, no. 5 (2025): 101322, https://doi.org/10.1016/j.xplc.2025.101322.

Supporting Information

Additional supporting information can be found online in the Supporting Information section.

Supporting File 1: admt70860-sup-0001-SuppMat.docx.